Nuclear Instruments and Methods in Physics Research A263 (1988) 136–149
North-Holland, Amsterdam

HADRON SAMPLING CALORIMETRY, A PUZZLE OF PHYSICS *

Hanno BRÜCKMANN, Bernd ANDERS ** and Ulf BEHRENS

I. Institut für Experimentalphysik der Universität Hamburg, Hamburg, FRG

The physics involved in hadron sampling calorimetry covers the wide energy range between high energy, medium energy, nuclear and atomic physics. All the processes contributing to energy depositions are discussed as well as illustrated by model calculations. The sampling fraction which determines the fraction of incident energy, which becomes visible in the detector layers, turns out to be strongly affected by the type of energy flow and the atomic number Z of the materials used. Normalized to mips, such fractions might range in the examples discussed between 0 and 2. Model calculations have been based on the HERMES scheme, which makes use of improved versions of the HET, the MORSE and the new developed DYMO code. The results allow to evaluate the degree of compensation and to predict e/h ratios. Such predictions agree quite well with the experimental results. In case of depleted uranium/scintillator sampling structures, compensation can be tuned by means of layer thicknesses. Finally, first results are presented for the investigation of fluctuations and correlations from model calculations evaluated event-by-event.

1. The topics of physics involved

In the forthcoming high energy experiments at CERN, DESY, Fermilab and similar facilities, detector physics has to cover energies up to the TeV range. With increasing energy, hadron calorimetry will be the most powerful tool to reveal new physics at such high energies.

1.1. Sampling, a paradox?

By applying the technique of sampling calorimetry to hadrons, one has to deal with energy deposited in the absorbed material (e.g. Fe, W, Pb, U) as well as energy deposition in the interleaved layers of the detector material (e.g. LA, scintillator, TMS, TMP). Energy deposited in the absorber is of course invisible. Hence the determination of incident energy has to rely completely on measuring only a small portion of energy visible in the detector layer.

At first glance it looks likely to characterize the percentage of energy deposition in the detector layers in relation to the energy absorbed in the whole heterogeneous sandwich structure by a sampling fraction. Such fraction might be convenient for dealing with the integral response. But it has to be pointed out very clearly that a single sampling fraction does not hold in general for the variety of processes involved. In case of a high energetic hadronic cascade, the total incident energy E_0 is distributed to very differently behaving particles like $e^{\pm}$, $\mu^{\pm}$, $\pi^{\pm}$, π^0, p, n, etc., and some energy might get completely lost via nuclear binding energy or neutrinos. The percentage in which energy becomes visible depends strongly on the special characters of energy transportation. It might look a paradox, but in consequence of the interactions involved sampling fractions differ considerably (table 1). Investigations have to account for the complexity of the situation.

An unambiguous sampling fraction can be given for fictitious mips, the minimum ionizing particles, traversing a sampling structure of specified materials. Mips deposit, independent of their energy, an average ionization energy $(dE/dx)_{mean}$. It is convenient to normalize the true energy depositions to the energy loss of the fictitious mips.

In fact even muons should not be used as an example for mips. Fig. 1 illustrates the mean energy loss for muons in bulk material of polystyrene and uranium [1]. At higher energies, bremsstrahlung, pair production and

Table 1
Typical average sampling fraction in calorimeters containing high Z absorbers (e.g. uranium).

Energy flow to	Sampling fraction
Mips (normalization)	1
Ionizing high energetic heavy particle tracks	1
Electromagnetic showers	0.6
Fission and n-capture γ's	0.3
Neutron kinetic energy: scintillator (saturation considered)	2
Liquid argon	≈ 0

* Supported by the Bundesministerium für Forschung und Technologie, BMFT, Bonn, FRG.
** DESY, Hamburg, FRG.

0168-9002/88/$03.50 © Elsevier Science Publishers B.V.
(North-Holland Physics Publishing Division)

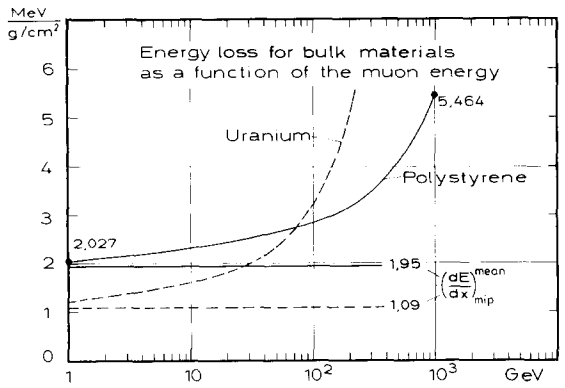

Fig. 1. The mean energy loss of muons in bulk material of polystyrene and uranium as a function of energy. The corresponding energy losses for minimal ionizing particles (mips) is given for comparison.

nuclear interaction are contributing so differently that the ratio of energy losses becomes energy dependent. Sandwich structures need a much more sophisticated treatment than bulk material.

1.2. The e/h ratio

The variation of the sampling fractions, according to the different particles and interactions involved, leads usually to different responses for electrons and hadrons incident on the calorimeter. As known from the literature, this ratio of responses (e/h ratio) might become as large as 1.5 and is in addition energy dependent [2]. An e/h ratio unequal to one gives unfortunately also a rise to a nonlinear hadron response to energy. This is simply due to the fact that with increasing incident energy, the π^0-production becomes much more dominating.

High energy calorimetry aimes at determination of jet-energies with the highest possible accuracy. Hence an optimal hadron sampling calorimeter should exhibit equal responses for electrons and hadrons (e/h ≡ 1). It is then called a fully compensated calorimeter.

1.3. Physics of compensation

Physics of calorimeter compensation deals with the energyflow, -deposition and -fluctuation in sampling geometries. For the absorber, high Z material is to be used preferentially. The following discussion and the examples concentrate on the use of uranium.

Five very different types of processes have to be distinguished to determine the characteristics of energy depositions.

(1) Energy deposition by (dE/dx)-ionization energy loss of charged particles like $\mu^{\pm}$, $\pi^{\pm}$, p, etc.

(2) Incident or internally created electromagnetic energy (γ, $e^{\pm}$, π^0), which gives rise to an electromagnetic shower.

(3) Release of neutrons in the MeV range, which might interact by elastic collisions or nuclear interactions.

(4) Fission processes of high Z nuclei, which might be directly induced by high energetic hadrons or by medium energy neutrons.

(5) Prompt nuclear gamma radiation emitted from the excited fission products or after particle evaporation from the residual nuclei. A source of delayed gamma radiation is the neutron capture process.

In fig. 2 the situation is illustrated. In combination with uranium, main emphasis is given to detecting layers of liquid argon (LA) and scintillator. Spallation, evaporation and fission of uranium is the source of neutrons as well as prompt gammas. Neutrons will first bounce a while with the nuclei contained in the structure to be finally captured by uranium predominantly. Compensation has to enhance the signal primarily produced by the high energetic charged particles and hence relies on the detection of some additional energy via neutron- and gamma-interactions. As can be already imagined the success will be strongly dependent on the choice of materials and geometry.

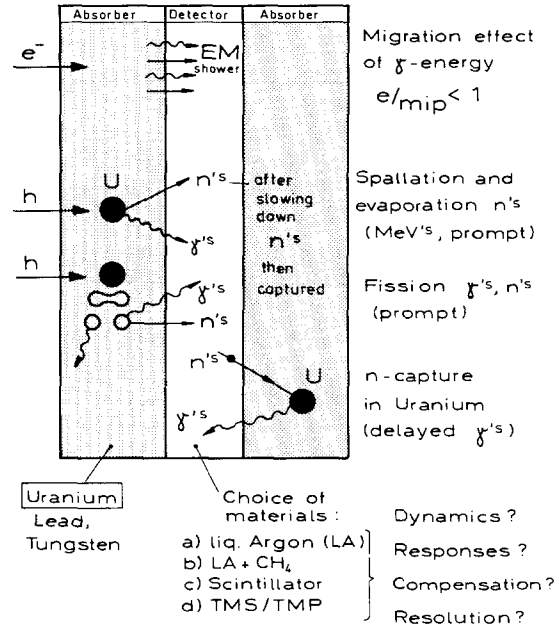

Fig. 2. The important effects, which are involved in the physics of compensating sampling calorimeters, are visualized schematically. The main emphasis lies on the production of neutrons and gammas in uranium absorber plates.

1.4. The five processes involved

The main features of the processes are to be summarized to ease the understanding of the results presented in section 3.

1.4.1. dE/dx of charged particles like $\pi^{\pm}$ and p

In between interactions the energy loss of heavy particles (e.g. protons) can be evaluated from the dE/dx-ionization. A purely ionizing track from protons created with equal spatial probability exhibits on average a normalized response of one (normalized to the response of mips). Thus the sampling fraction is identical to the mip sampling fraction. If charged pions are traveling along between interactions, the situation becomes somewhat more complicated. Corrections like the ones mentioned above for muons are to be considered. But an average normalized response of one might be justified for $\pi^{\pm}$ in first order.

1.4.2. Electromagnetic showers in a high Z sampling structure

Em-showers dissipate their whole incident energy E_0 finally in the layer structure. Energy is fluctuating between an electron and a photon component. Energy deposition is drawn from the electron component only. The branching ratio of energy deposited in the absorber- and the detector-layers depends on the Z of the materials involved. Hence em-sampling fractions might turn out to be quite different from the corresponding mip sampling fraction. For a stack with high Z material the response normalized to mips was experimentally found to be much smaller than one [3]. Some numerical results obtained with the EGS code are published [4–7]. The general explanation in terms of physics are already presented [8]. Some of the main features have been discussed independently [5]. Briefly summarizing the situation, it is to be pointed out that a reduction of the em-response in high Z sampling structures is not at all due to the "transition effect" discussed in ref. [9]. Consequently a different name – migration effect of γ-energy – was proposed in ref. [8] to characterize the effect in sampling calorimetry. Fig. 3 illustrates the situation. Mips are branching their energy according to the mip sampling fraction (indicated by a full line). The flow of photon energy (MeV range and below) dissipates energy via pair production, Compton effect and photoeffect. In case of high Z absorbers, photon energy migrates predominantly into the absorber. This is mainly due to the photoeffect, which is proportional to the fourth to fifth power of Z. The dashed lines in fig. 3 indicate the amount of energy released by the flow of photons. The effective detectable em-signal is a mixture of photon and electron energy dissipation. Because the migration effect favours the energy deposition in the absorber, high Z calorimeters show an em response

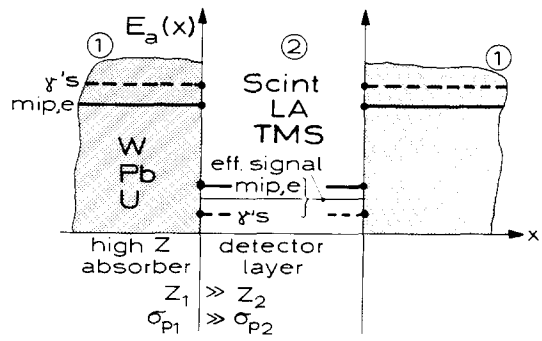

Fig. 3. The migration effect of γ-energy is shown schematically for an em-shower, passing through a sampling structure (#1 absorber, #2 detector and $E_a(x)$ energy absorber per unit of length). Example: A geometry, which has a mip sampling fraction of 7% and 2% sampling fraction for the low energy gamma component of the shower exhibits an em overall sampling fraction of 4.2%.

which is considerably smaller than the mip response. Hence the e/mip ratio is smaller than one. The influence of the migration effect is not much affected by the energy of the incident electron. The mixing ratio in the shower between mips and interacting γ's does not change significantly with incident energy. Such a small energy dependence of the e/mip ratio has been observed in EGS calculations [6].

Using the EGS code, e/mip ratios have been obtained for scintillators with U, Pb, Fe and Cu absorber layers (fig. 4). In fig. 5 the situation for liquid argon (LA) with U, Pb and Cu absorbers is shown. As indicated in the figures, these results were obtained by using standard cuts (ECUT = AE = 1.5 MeV and PCUT = AP = 0.1 MeV) and the default step size algorithm from the EGS code. It has been pointed out by Rogers [10] that very accurate EGS calculations need for optimisation the use of much lower cuts and an adjustment of the step sizes. Otherwise, in case of many thin layers, interface artefacts can spoil the accuracy of the calculation considerably [11]. A continuous decrease of the step size parameter in the program results in steadily increasing e/mip ratios. Changes of up to 10% might be obtained in comparison to the numbers given in figs. 4 and 5. On the other hand, practical calorimeters might have a metallic cladding layer on the absorber sheets. This affects the e/mip ratio by a decrease of up to 10%. This can be understood in terms of shielding electrons on their way between the high Z absorber and the detector layer. Detailed investigations using the improvements given in refs. [11,12] are in progress and will be reported elsewhere.

1.4.3. Creation and interactions of neutrons

As illustrated in fig. 6, neutrons might be produced

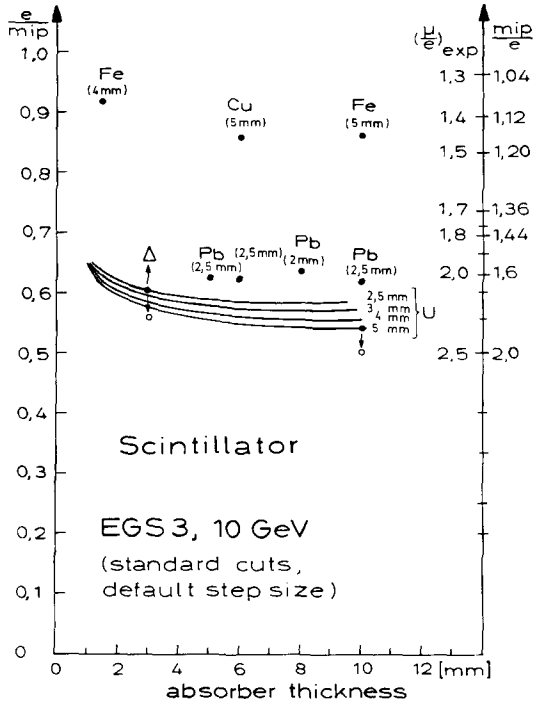

Fig. 4. e/mip ratios for various absorber and scintillator thicknesses. A slight dependence of e/mip with the scintillator thickness is revealed. The open circles give the result for cladding the absorber sheets (2×0.4 mm Cu for the 3 mm U-sheet and 2×1 mm Fe for the 10 mm U-sheet). The △ symbol belongs to an EGS calculation, using nonstandard cuts (ECUT = 0.711 MeV, AE = 0.700 MeV and PCUT = AP = 0.1 MeV) and a step size parameter ESTEPE = 0.5%. On the right scale, the mip/e-ratio is compared to an $(\mu/e)_{exp}$ ratio expected for 10 GeV muons.

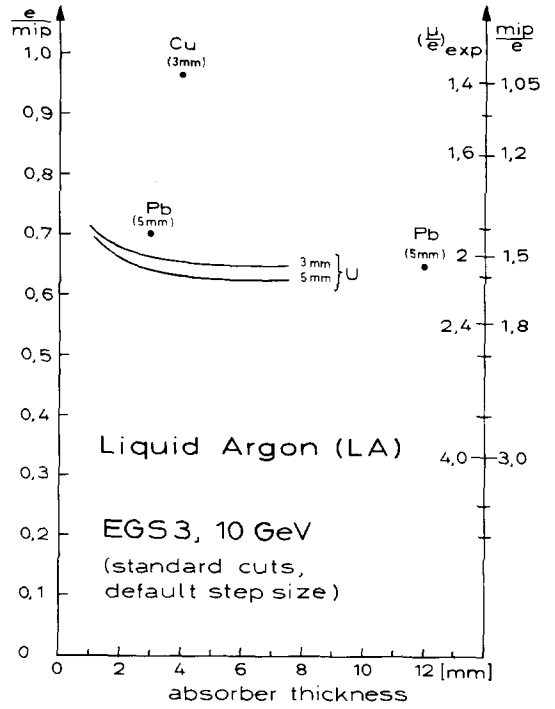

Fig. 5. The e/mip ratios for liquid argon detector layers and various absorber materials. By comparing with fig. 4, one observes that the higher Z material (LA) increases the e/mip ratio. This is due to a photon detection efficiency which increases with the Z of the detector layer. On the right scale, the mip/e ratio is compared to an $(\mu/e)_{exp}$ ratio expected for 10 GeV muons.

either by spallation of high Z nuclei or – in case of fissionable material – be evaporated from the highly excited fission products. The few very highly energetic neutrons created will travel some distance through the stack and then indicate a further spallation. They behave rather similarly to the charged highly energetic hadrons.

Most of the neutrons are created in an energy range between 0.1 and 10 MeV by nuclear evaporation. The spectra and the method of calculation are discussed in section 2. For understanding the response to neutrons in a sampling structure, one has to consider their mean free path. Fig. 7 illustrates the total cross section of natural uranium, the fission cross section of ^{238}U, the (n, γ) capture cross section of ^{238}U and the n–p elastic cross section in the energy range from 10 keV to 100 MeV. The neutron mean free path ranges between 2 and 5 cm typically, as can be evaluated from the cross sections and a weighted material composition. Therefore in the energy range considered, neutrons are not

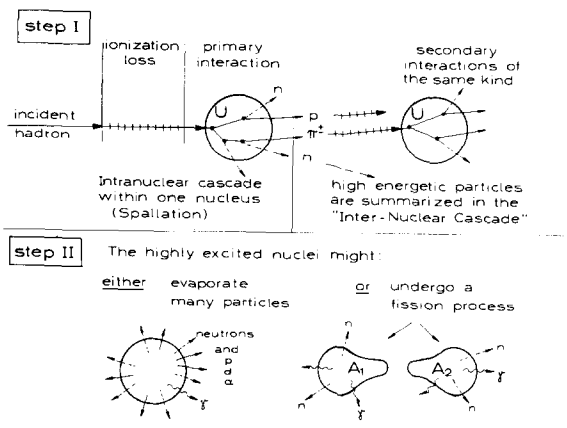

Fig. 6. Step I: Development of an "internuclear cascade". From one nucleus an intranuclear cascade releases a few high energetic spallation products, which are able to iniciate further intranuclear cascade processes. Step II: The highly excited nuclei remaining from each intranuclear cascade deexcite.

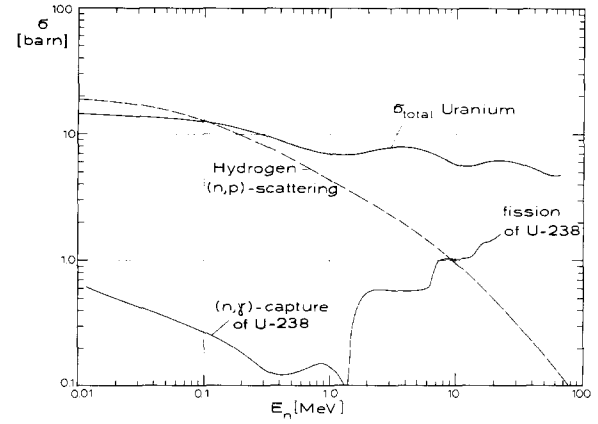

Fig. 7. Cross sections for neutron induced reactions on uranium and hydrogen.

much affected by single layers of the alternating material composition in a sampling calorimeter (3–5 mm). Neutron transport is governed by the mean parameters of the whole material mix predominantly. Material mixes containing an appreciable amount of hydrogen (organic scintillators, TMS and TMP) have to be clearly distinguished from mixes which contain medium A and high A materials only. In mixes with hydrogen content, neutrons will deliver almost their whole kinetic energy in rather few and large steps to recoiling protons. Such an energy conversion mechanism which creates such large detectable recoil energies is absent if the detector contains only medium and high A material (e.g. liquid argon). The conversion efficiency of proton recoil energy to signal is strongly affected by saturation effects in the detector material. In case of organic scintillators, such saturation is described by the kB-parameter in the Birk's formula [13]. kB has a value of somewhat below 1×10^{-2} g/(cm^2 MeV), typically. By summarizing, one recognizes that the sampling fraction for neutron kinetic energy can be made much larger than the mip sampling fraction.

1.4.4. The contribution from fission processes

As indicated in fig. 6, spallation might be followed by a fission process or, as can be seen from the cross section given in fig. 7, fast neutrons might induce a fission process as well. Both reactions produce two highly excited fission products. Although most of the binding energy released by fission shows up as kinetic energy of the fission products, this energy does not contribute to the signal. Because of the extremely short range (≈ 10 μm) of fission products, this energy is dissipated within the absorber plates.

Besides the neutrons discussed above, energy released promptly by deexcitation gammas is the only part which can contribute to the signal. As will be seen from the results of calculations, γ-detection efficiences are low and the contributions to the signal turn out to be rather small [14].

1.4.5. The delayed (n, y) capture process

Besides the prompt fission gammas mentioned above, γ-radiation is produced by the capture of neutrons. The cross section for (n, γ) process gets large in the range of neutron energies of several keV (resonance region) and very large at even lower energies (eV to thermal energies). Consequently, delayed contributions from the detection of the capture-gammas are arising. Neutrons have first to be slowed down in energy (moderation). The dynamics of neutron moderation depends on the material mix in the calorimeter. For fast moderation a hydrogen content is most favourable.

Capture gammas contribute to the signal only with efficiencies which are as small as in the case of the prompt fission gammas. Hence the sampling fraction for this kind of energy release is very much smaller than the mip sampling fraction.

2. The computer code system HERMES

The simulation of all the different processes involved needs combining results from several large codes which are properly adapted to special parts of the problem. The organisation scheme of HERMES (High Energy Reaction Models for Elaborate Simulations) is shown in fig. 8. Incident hadrons are first treated with the 3-dimensional HET-KFA code [15]. This code is an improved version of the Oak Ridge analog Monte Carlo code HETC [16]. The result of such a computation is dumped, for keeping track of history, on an event-by-event basis on a mass storage device. Concerning the neutron production, highly energetic neutrons ($E_n > 15$ MeV) are consequently transported with the HET-KFA code. Only neutrons produced with energies below 15 MeV are intermediately stored to be either transported with codes like MORSE [17] or ANISN [18] or to be used as an input to the DYMO code [19,20].

MORSE, originally developed by ORNL as a group Monte Carlo program to calculate neutron and gamma transport for radiation shielding and dosimetry problems, is a 3-dimensional code system, using the so called combinatorial geometry input to deal with real objects in space.

The code DYMO was implemented for the special purpose to calculate the dynamics of sampling calorimetry.

ANISN is the ORNL multigroup one-dimensional discrete ordinates transport code system with anisotropic scattering, which can be used to transport neutrons as well as gamma radiation. This is achieved by solving iteratively the Boltzmann equation.

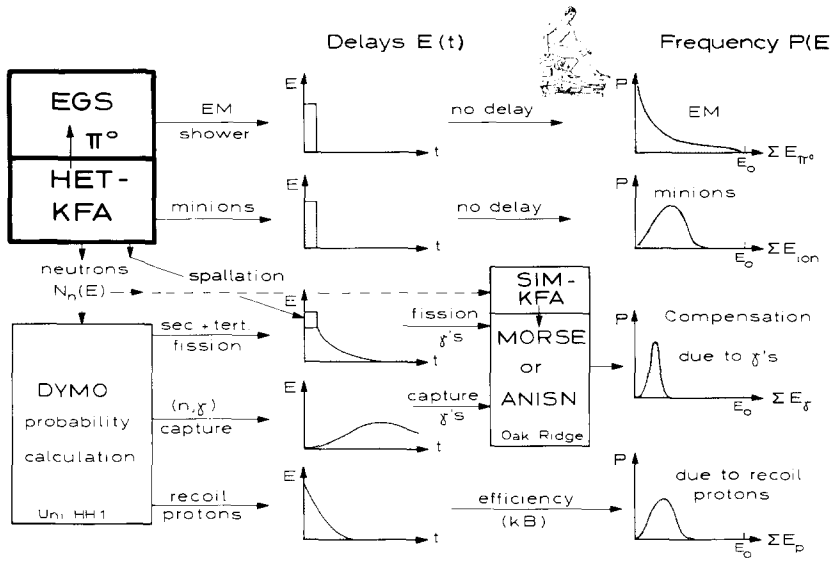

Fig. 8. The organization scheme of the HERMES (High Energy Reaction Models for Elaborate Simulations) code.

For all three codes energy spectra for neutrons and gammas are properly binned into groups. Group-to-group transfer probabilities are extracted from a huge nuclear data library for each energy group. This library is based on experimental data and contains for all nuclei the relevant neutron and/or gamma reactions [21]. We have used so far the DLC31 (or FEWG1) library [22], which covers 37 neutron groups (10^{-5} eV $\leq E_n \leq$ 20 MeV) and 21 gamma groups (10 keV $\leq E_\gamma \leq$ 14 MeV).

As illustrated in fig. 8, the different components of energy flow have different delays $E(t)$, characterizing the function of time according to which energy is able to show up visible. Em-showers and the dE/dx energy loss of minimal ionizing hadrons produce immediately visible energy. Prompt fission γ's are either produced if a spallation process is followed by fission or might be generated with some delay, if fission is induced by one of the fast neutrons in the MeV range (secondary and tertiary fission). The creation of capture γ's is considerably delayed, because the neutrons have to be slowed down to very low energies. The generation of visible energy via production of recoil protons is correlated to the moderation of the neutrons. Therefore this contribution is also time dependent.

In spite of the importance of dynamics, some features of the DYMO code are to be summarized. The code operates from any input neutron spectrum ($E_n^{max} \leq$ 20 MeV) on the basis of group-to-group probabilities in the homogeneous material mix of the calorimeter (mean free path of the neutrons much larger than layer thicknesses). DYMO uses small steps of time (typically 0.1 ns) to evaluate the numbers of neutrons being either affected in their energy or lost to fission or capture. After each step in time all the 37 neutron energy groups are updated in content. This includes a gain of neutrons by secondary fission. DYMO keeps continuously track of the neutron spectrum versus time as well as produces transition rates to all reactions specified. This way, the abundances of the various nuclear gamma sources are determined versus time. By using such abundancies, which are allocable to materials in the layer structures, γ-efficiencies for visible energy production become calculable with the ANISN or MORSE code.

The last column in fig. 8 illustrates, how a degree of compensation is finally to be evaluated by summing up all the visible energy within a given gate time.

The discussion of the HERMES scheme up to this point connects average features of the processes only. Calculations carried out in such a sequence are able to deliver predictions for e/h ratios and compensation (see figs. 16 and 17).

To study the fluctuations on an event-to-event basis, the output of the HET-KFA code has to be directly coupled to an improved analog MORSE code [23] (dashed line in fig. 8). Although CPU time tends to explode, visible energy is then reconstructable from all its components for each event.

3. Results and discussion

The neutron yield for π^- incident on a block of depleted uranium (DU) has been calculated, using the HET-KFA code [15]. The yield of neutrons per incident π^- multiplied by the neutron energy, results in a lethargy

plot (1 lethargy = ln(10/E)), shown in fig. 9. This kind of plot is convenient because areas under the curves are proportional to the total number of neutrons produced. Normalization is illustrated by the small dashed area which corresponds to 10 neutrons produced. In the case of DU each incident π^- produces in average of 326 neutrons with $E_n^{max} \leq 20$ MeV. For comparison a Maxwell spectrum is shown with $kT = 1.3$ MeV, normalized to the same number of neutrons (dashed line). The Maxwell spectrum describes the energy distribution of neutrons from secondary or tertiary fission, induced by neutrons in the MeV range. Neutrons being evaporated on the tail of an intranuclear cascade process have on average higher energies. Hence the π^- indicated spectrum is shifted to higher energies. Fig. 9 shows additionally the neutron spectrum for 10 GeV π^- incident on lead. Although lead is not fissionable by MeV-neutrons, the intranuclear cascade produces neutrons with a spectrum which is very similar in shape. But one incident π^- releases on average only 222 neutrons. The comparison of the yields illustrates the ease of compensation which is obtainable by using uranium. Still in respect to future calorimetry in the range of several TeVs, the lead case should be studied in much more detail by investigating also second order effects favouring an enhancement of compensation ability.

To evaluate the time dependence of the significant process, the DYMO code is started with the primary n-spectrum of fig. 9. As an example the result of dynamics is shown in fig. 10 for an uranium/scintillator stack. It should be explicitely noted, that the time is plotted in fig. 10 on a logarithmic scale. By using

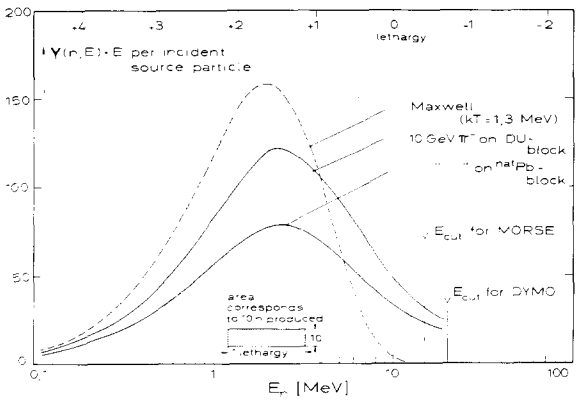

Fig. 9. The spectral neutron yields $Y(n, E)$ per MeV and per incoming 10 GeV π^- incident on an uranium or lead block, respectively. Plotted is the product $Y(n, E) \cdot E$ versus the lethargy of the neutron energy (upper scale). The 3-dimensional HET-KFA MC code was used. The block sizes were $60 \times 60 \times 300$ cm each. The spectra shown are used as input for calculations with either DYMO, MORSE or ANISN.

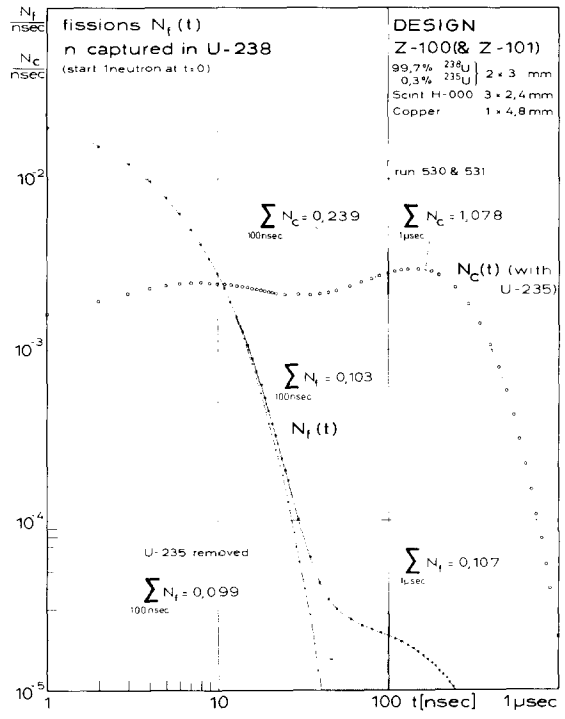

Fig. 10. The number of secondary or tertiary fission $N_f(t)$ and the ^{238}U neutron-capture $N_c(t)$ versus a logarithmic time scale. Integral numbers after 100 ns and 1 μs elapse of gate time are added for comparison. The properties of the hypothetical scintillator H-000 are similar to the conventional ones on polystyrene basis. The C : H ratio is 1 : 1.

depleted uranium (DU) and starting 1 neutron at $t = 0$, one will observe a sum of 0.103 fissions in the first 100 ns and 0.107 fissions, if waiting e.g. 1 μs. As can be seen from the dashed area, most of the rather late fissions are due to the very small content of ^{235}U (fissionable only with very low energy neutrons). The neutron capture of ^{238}U is additionally plotted in fig. 10. In consequence of a small contribution from secondary and tertiary fissions, the starting single neutron yields on average 1.078 captured neutrons after 1 μs. The expectation to find more by waiting longer is negligible. By looking at the 100 ns sum, one finds 0.239 neutrons captured only. This low value is due to the energy dependence of the capture cross section discussed above. The results of such calculations are to be compared in detail with experimental data [25] available meanwhile.

To entangle the significance and contributions of the different processes, fig. 11 shows as example a lethargy plot of the result for a DU/cladding/scintillator ZEUS design. Plotted is the visible energy per ns multiplied by the time. Hence areas under the curves are proportional to absolute amounts of visible energy. The dashed area

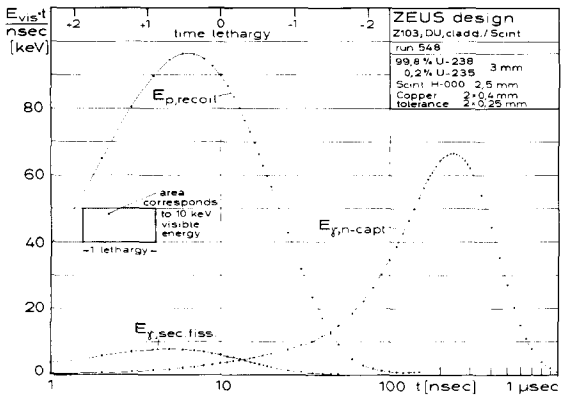

Fig. 11. The contributions to "visible" energy from proton recoils and from the nuclear processes. In the lethargy-plot, areas are directly proportional to an amount of energy contributed.

shows the normalization of area to 10 keV visible.

The saturation effect of the scintillator was included in the evaluation of the visible proton recoil energy $E_{\mathrm{vis}}\ (t)$. A value of $\mathrm{kB} = 0.85 \times 10^{-2}$ g/(cm^2 MeV) was used [19,24].

The gamma energy which is released during the fission process and the neutron capture reaction is converted to visible energy with a very small efficiency only. Calculations carried out with ANISN yield 2% detection efficiency [14]. As has been discussed, this is to be compared with nearly 7% mip sampling fraction in this geometry.

As is readily seen in fig. 11, the proton recoils produce the dominating contribution within the first 100 ns. Later on some additional signal arises from (n, γ) capture in ^{238}U. To illustrate the expected compensation contribution versus gate time, in fig. 12 the result obtained by integrating the curves of fig. 11 is shown.

As has been already proposed in ref. [8], it is convenient to express the mean values of compensation in additive terms:

$$C = C_{\mathrm{recoil}} + C_{\gamma,\mathrm{prim.fiss.}} + C_{\gamma,\mathrm{sec.fiss.}} + C_{\mathrm{delayed}\,\gamma}\,.$$

The quantity C characterizes the degree of compensation. The normalization is chosen such that $C = 1$ corresponds to full compensation and hence to e/h = 1. The experimentally measurable ratio e/h can then be written as:

$$\mathrm{e/h} = \frac{\mathrm{e/mip}}{\dfrac{h_i}{\mathrm{mip}} + C\left(\dfrac{\mathrm{e}}{\mathrm{mip}} - \dfrac{h_i}{\mathrm{mip}}\right)}\,;$$

e denotes the energy deposition in the detector by a pure electromagnetic shower. h_i denotes the energy deposition of the ionizing part of the hadronic shower which contains hadronic as well as electromagnetic components. The definition of C and the relation between e, h_i, mip and C is illustrated in fig. 13 schematically. A more detailed illustration of h_i is presented in section 4.

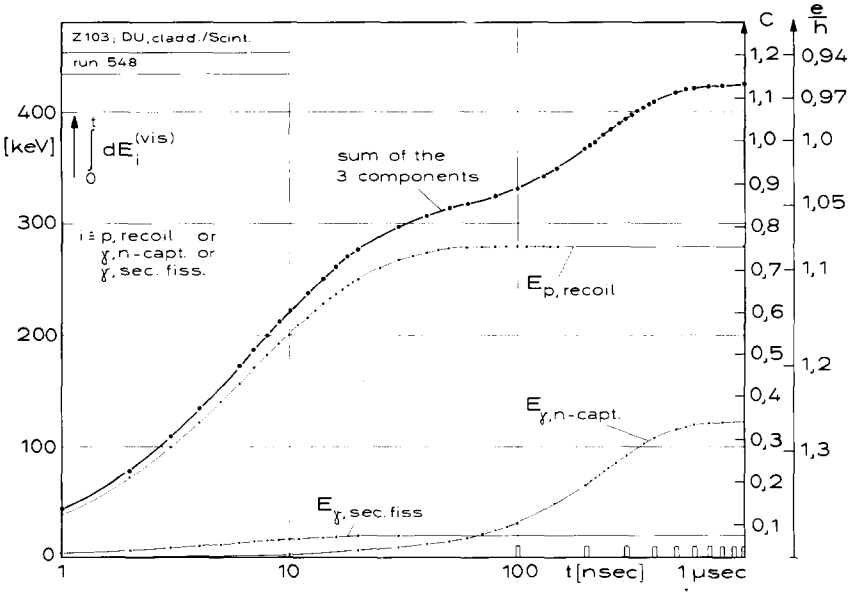

Fig. 12. The visible energies $E_{\mathrm{vis}}(t)$ from fig. 11 integrated over time. The compensation contribution expected can be read versus gate time. An e/mip = 0.60 was taken from an EGS calculation which included the cladding and used a nondefault step-size parameter ESTEPE = 0.5%.

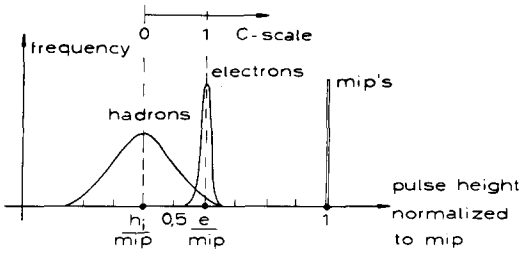

For comparing U/LA stacks with U/scintillator stacks, some results of calculations which had been reported previously [8] are given here in identical scales in figs. 14 and 15. Missing the p-recoil contribution, the compensation signal becomes very slow and insufficient in total amount.

Fig. 13. The definition of the C-scale as a convenient measure of the degree of compensation.

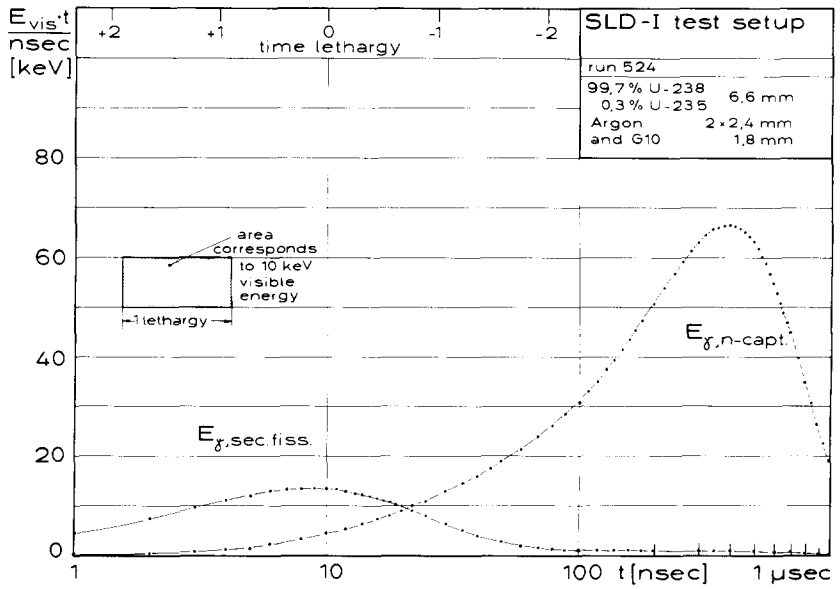

Fig. 14. Lethargy-plot of $E_{vis}(t)$ for an uranium/liquid argon layer structure. For ease of comparison, scales are identical to fig. 11. Although fission contributes somewhat more compared to the scintillator case, the main nuclear contribution in LA is due to the late n-capture process.

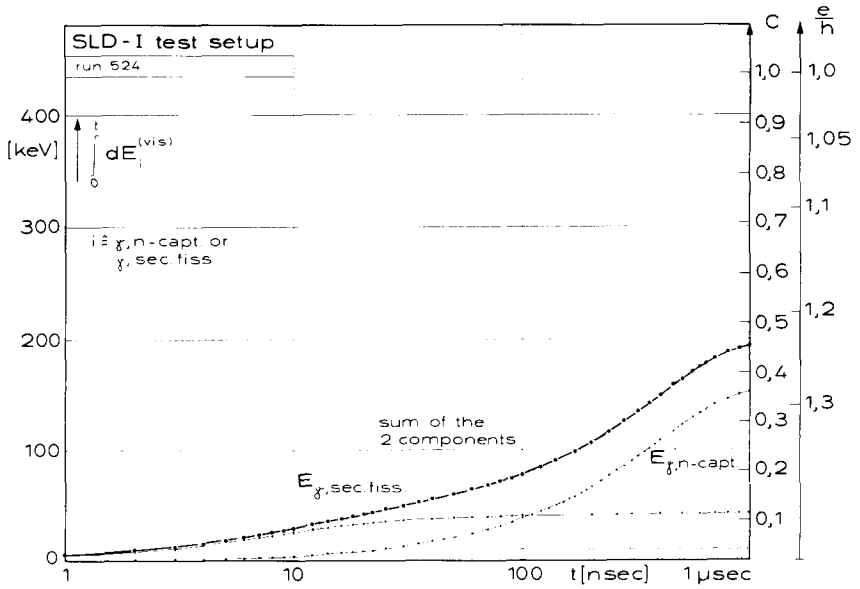

Fig. 15. The visible energies from fig. 14 integrated over time. Scales are identical to fig. 12. Even at 1 μs gate time, a contribution of only 50% of compensation needed can be achieved.

4. Tuning of compensation

Systems which behave like the DU/scintillator setup discussed above (DU/TMP is expected to be similar) have an unique feature for tuning the compensation to e/h = 1. Results of calculations are presented in fig. 16 to illustrate the situation. The degree of compensation C is plotted versus the ratio of thicknesses of the DU plates and the scintillator plates. Restricting the discussion to usual layer thicknesses in the range of a few millimeters, C is dominated by the thickness ratio d_u/d_s. Only second order effects like some loss of recoiling protons at the scintillator surface and a slight change of the e/mip ratios with thicknesses (see fig. 4) distinguish 2.5 and 5 mm scintillator layers at a fixed ratio d_u/d_s.

The range of $C < 1$ corresponds to undercompensation whereas $C > 1$ characterizes overcompensation of the calorimeter. The favourable situation where the compensation is adjusted to $C = 1$ is indicated by a dasher bar.

The tuning of compensation [8] by means of layer thicknesses can be accomplished only in calorimeters which contain hydrogeneous material (scintillator, TMS, TMP) in the detector layer. The reason for such tuning feature is to be seen in the fact that the neutrons deliver their whole kinetic energy to the hydrogen in the detector layer predominantly (this sampling fraction is almost independent of the layer thicknesses). Consequently the absolute amount of compensation signal from neutron kinetic energy is to first order constant, whereas the height of the signal which is to be compensated, decreases with decreasing detector layer thickness. (Decrease of sampling fraction for ionizing tracks of particles.)

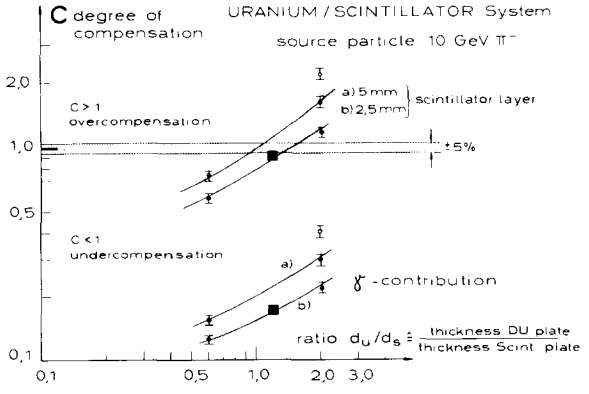

Fig. 16. The degree of compensation C for a uranium/scintillator system. A tuning can be achieved by varying the thickness ratio. A weak dependence on the scintillator thicknesses is mainly due to a slight change of the e/mip ratio shown in fig. 4. Calculations have been carried out with a kB value of 0.85×10^{-2} g/(cm² MeV). The error bars given have been estimated from the Monte Carlo statistics. The open circle denotes the result of a calculation with a 2×1 mm Fe cladding on the uranium layers to compare with the WA78 experiment.

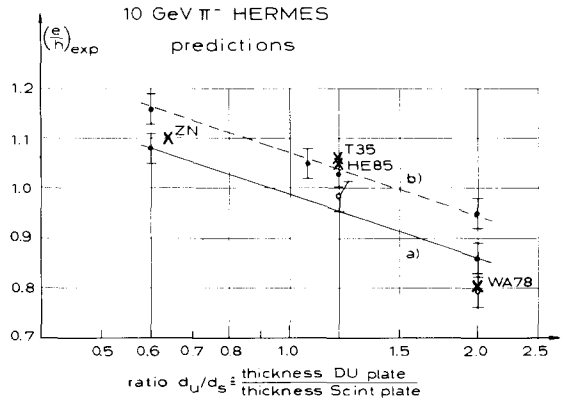

Fig. 17. e/h ratios from experiments are compared with HERMES predictions, based on mean value calculations. Curve (a) corresponds to 5 mm and (b) to 2.5 mm scintillator thickness. The open circle at the thickness ratio 1.2 corresponds to a 2×0.4 mm Cu cladding, the open circle at 2.0 to a 2×1 mm Fe cladding. Standard cuts and the default step-size algorithm from EGS have been used throughout.

To compare with experimental data the calculated degree of compensation C is to be expressed in terms of e/h ratios. Fig. 17 shows such predictions (small dots) for 10 GeV π^- incident on DU/scintillator stacks of various thickness ratios. Changes which are predicted for a cladding of the DU are indicated by small circles. Experimentally determined e/h ratios are given for comparison. They are plotted as crosses labelled by ZN (ZEUS/NIKHEF-Test) [26], HE85 (HELIOS 85) [27], T35 (ZEUS-Test 35) [28] and WA78 [29]. In the case of the WA78 experiment, the uranium plates had been mounted in steel frames and covered by 1 mm steel plates. Hence the experimental value is to be compared to the prediction which includes this cladding (open circles).

The ZEUS-Test 35 was performed at the CERN-PS in summer 1986 using DU plates of 3 mm thickness and 2.5 mm thick SCSN 38 scintillator sheets. Measurements have been carried out between 3 and 9 GeV/c. The average energy resolution for hadrons [28] was measured as $\sigma/E = 33.5\%/\sqrt{E}$. The e/h ratio determined experimentally for a 200 ns gate width was e/h = 1.06.

5. The use of uranium with different detectors

For comparing compensation features of several detector materials, calculations have been carried out for pure liquid argon, LA with CH_4 added in 7.5% of

Table 2

	LA pure	LA + methane	TMS	Scintillator
Geometry [mm]	6.6 DU 1.8 G10 2×2.4 LA	6.6 Du 1.8 G10 2×2.4 LA 7.5 wt.% CH_4 added	6.6 DU 1.8 G10 2×2.4 TMS	3 DU 2×0.4 Cu 2.5 scint. (H-000)
e/mip	0.63	0.63	0.63	0.60
h_i/mip	0.41	0.41	0.41	0.41
amends needed for full compensation [MeV]	144	144	95	125
If waiting 1 μs energy visible from:				
γ's → prompt fission [MeV]	17	12	6	10 [a]
γ's → n-capture [MeV]	52	46	27	10 [a]
Sum from γ's [MeV]	69	58	33	20 [a]
Kinetic energies of neutrons (recoil p) saturation [MeV]	–	81	64	91 [a]
kB [g/(cm² MeV)]	–	0.45×10^{-2}	1.4×10^{-2}	0.85×10^{-2}
Degree of compensation C [%]	48	97	102	89
e/h	1.22	1.01	0.99	1.04

[a] Waiting 100 ns only.

weight, TMS and scintillator. Table 2 summarizes the results obtained. From figuring out the e/mip ratio and by use of a h_i/mip ratio of 0.41, in a first step the amends needed for full compensation ($C = 1$) are evaluated. In the second step the average energy which becomes visible in 1 μs or 100 ns, respectively, is evaluated for each kind of compensation contribution. In table 2 the energies are listed, which become visible from prompt fission gammas, neutron capture gammas and from the kinetic energy of the neutrons created. By comparing the amends needed with the sum of all the contributions, one arrives at the degree of compensation C and at predictions for e/h ratios. As is readily seen, pure LA is not able to compensate because of the lack in detecting the kinetic energy of neutrons. An addition of a considerable amount of methane would be needed to achieve full compensation. TMS and TMP are predicted to compensate readily as long as charge recombination stays small enough and thus allows for detecting the recoil protons with high efficiency (kB value needs to be verified experimentally, the value given by ref. [20] was used).

6. The treatment of fluctuations

An evaluation of mean values as discussed above does allow only to understand the relative changes in calorimeter hadron resolution which are due to a change of the average degree of compensation or the overall e/h ratio, respectively.

A detailed analysis and understanding of the effects of the fluctuations involved has, clearly, to start with a study on how energy is distributed within single events. By using the HERMES scheme for evaluating event-to-event fluctuations, one is able to arrive at predictions for absolute values of hadronic resolutions in sampling calorimeters.

The whole energy supplied by one incident particle is distributed to many different reaction channels. As discussed at the beginning, sampling fractions depend strongly on the special character of energy flow. Therefore each such reaction channel exhibits its own partial response.

Fig. 18 schematically shows the possibilities for distributing energy. Within the hadronic cascade firstly several π^0's might be produced. Their total energy altogether populates the em-channel. This part of the

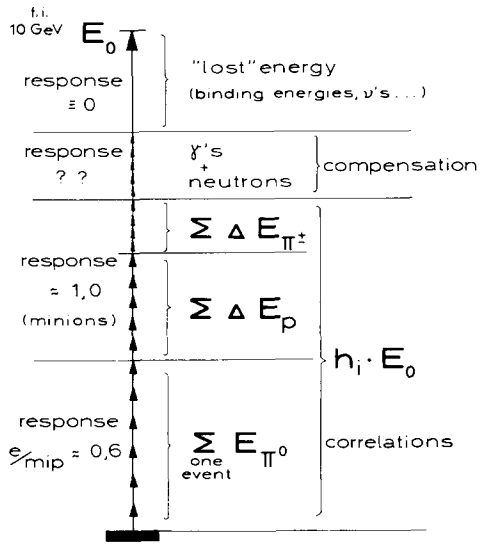

Fig. 18. The main components of event-to-event fluctuations in hadron sampling calorimetry. Each component exhibits its own characteristics and has its own partial response.

energy is detected with a partial normalized response of approximately 0.6 (see fig. 4). Secondly, all the highly energetic charged pions and the protons created might travel some distance through the structure before interacting again. Energy is dissipated by such minions in the form of (dE/dx)-ionization. The partial normalized response is 1.0. Thirdly a huge number of neutrons and gammas is created by spallation, fission and nuclear reactions. The partial response to the kinetic energy of neutrons might be rather high (e.g. 2 for scintillator layers), whereas the response to nuclear gamma radiation is rather low (see table 1). Last not least, some part of the total energy will disappear, e.g. in the form of nuclear binding energy or neutrinos. Here the partial response is zero per definition.

Although one has to keep in mind enormous fluctuations between populating these channels, calorimetry still aims at determining the incoming total energy with optimum resolution. Because the normalized partial responses are ranging between zero and two, the task is exceptional and elaborate. One has to try to reveal correlations. The procedure to be followed is explained stepwise. Fig. 19 shows a correlation plot for 10 GeV π^- on a block of uranium. Dealing with particle production, detector layer materials can be neglected in first order. In such a scatter plot, two coordinates belong to each single event. The abscissa corresponds to the total π^0-energy, which was produced by all the π^0's created in the event. The ordinate corresponds to the sum of the (dE/dx)-ionization energy, which is spent by all the highly energetic charged particles on their travel between interactions. Although unrealistic, let us assume first an equal response to both kinds of energy. Then both axes are to be weighted by the response 1, as illustrated in fig. 19. If the whole total incident energy E_0 of an event would flow completely to π^0's and ionization, then the event would be located on the 45°-line marked by $E = \text{const} \triangleq 10$ GeV. As illustrated, the HET-KFA calculation shows that all events are located far below this 10 GeV = const. line. But they are still correlated in such a way, that they group around a straight line with much smaller slope. The shape of the pulse height spectrum which one would observe is determined by adding the energies of the abscissa and the ordinate. Equivalently one may simply look at the projection onto the pulse height axis PH. The mean value of such spectrum in fig. 19 would correspond to the value h_i defined in section 3. But so far neither compensation nor reduced response on the abscissa (migration effect) is taken into account.

To arrive at the realistic situation, it has firstly to be accounted for a mip sampling fraction to incorporate the geometry of the layer structure. Both axes have to be rescaled. Secondly, the reduced response to em energy is considered by weighting the abscissa with the e/mip ratio. For illustration, a value of 0.6 is taken. The result is shown in fig. 20. The quantity h_i has now again to be evaluated from the projection onto the PH-axis and is now the realistic one to be used for compensation predictions.

It is important to realize that an incoming electron would give a signal, which can be found in the plot at the position marked by the e^--dot on the abscissa. The

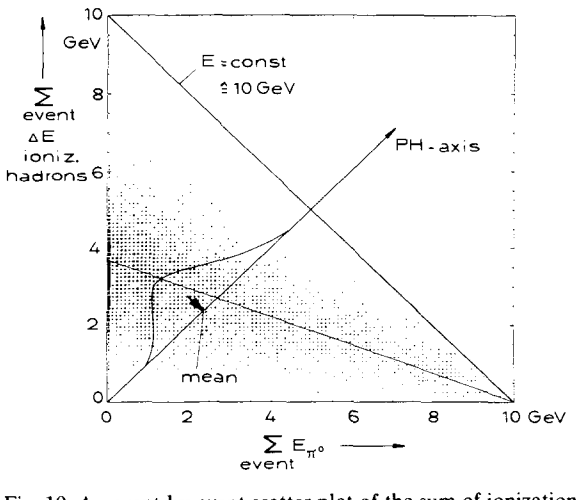

Fig. 19. An event-by-event scatter plot of the sum of ionization energy of all the charged hadrons versus the sum of the π^0-energy per event. HET-KFA Monte Carlo results for 10 GeV π^- incident on a uranium block of $60 \times 60 \times 300$ cm size. The migration effect for the em-energy is intentially included in fig. 20 only.

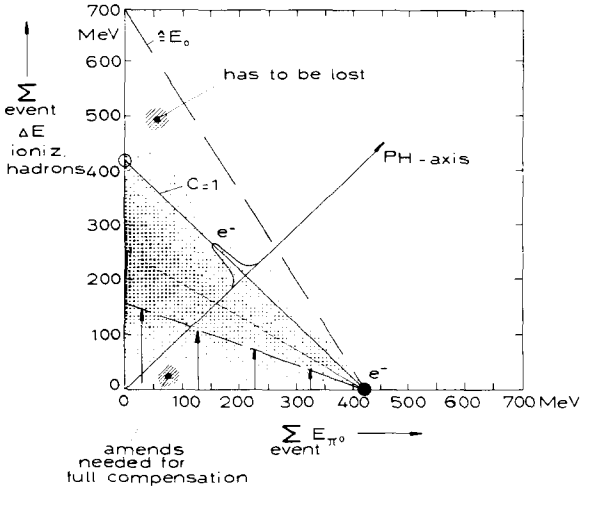

Fig. 20. The correlation plot of fig. 19 rescaled to the case of a sampling calorimeter with a mip sampling fraction of 7% (corresponding to 3 mm DU/2.5 mm scintillator layers) and an e/mip ratio of 0.6. The line of equal response to electromagnetic as well as hadronic signals – full compensation – is indicated by $C = 1$.

45° connection of this point with the analog one on the ordinate gives the straight line, labelled $C = 1$. Compensation would be achieved if the events would group symmetrically around this 45° line. If such a grouping around the $C = 1$ line is achieved, then the projection onto the PH-axis would have the smallest width. Hence the hadrons would be detectable with optimum resolution.

Clearly, one needs correlated amends from neutrons and gammas to achieve the optimal situation of compensation. The amends needed in this example are indicated by arrows at the bottom of fig. 20. It is interesting to note that compensation does not mean at all to make amends to reach the full incident energy E_0. As is illustrated in fig. 20, some energy has to be lost and one could also express compensation by stating "just loose from E_0 the correct and correlated amount of energy".

Fig. 21 shows the result of a first attempt to simulate the hadronic cascade with the HET-KFA code including the contributions from detection of proton recoil energies with an improved version of the MORSE code [23]. This result was obtained for a stack of 107 layers of DU (3.2 mm) and 107 layers of scintillator (2.5 mm). The lateral size of the stack used was 60×60 cm^2. In this first attempt, contributions from deexcitation gammas have not been added to the abscissa coordinates of the events. But for 100 ns gate width, an inclusion of the gammas will produce only a slight smearing in the direction of the abscissa, because the sampling fraction of the gamma contribution is 0.3 only in respect to mips. Although the stack used in the simulation was not yet deep enough in λ, a compensation by neutron kinetic energy and hence a grouping around the $C = 1$ line is clearly visible. The use of this method in further model calculations will give detailed insight into the significance of fluctuations and correlations.

7. Summary

The physics involved in hadronic sampling calorimetry covers an energy range from TeV down to eV. High energy physics, medium energy physics, nuclear physics as well as atomic physics are needed to understand the complexity of processes, which govern the branching of energy depositions into absorber and detector layers. The specific sampling fractions depend on the type of energy flow, on the materials used and on the geometry of the layer structure.

Fig. 22 summarizes the main effects which are to be considered in solving "the puzzle" and explaining the physics of hadron sampling calorimetry. Compensation is needed to achieve optimum energy resolution and equal responses to electrons and hadrons. The use of depleted uranium as absorber and detector layers with high hydrogen content is by now the optimal combination. These materials allow even with ease a tuning to full compensation, because plenty proton recoil energy can be made available via neutrons released from uranium.

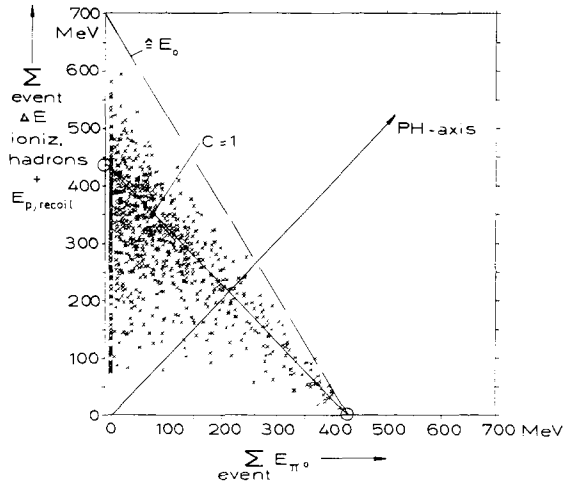

Fig. 21. The visible proton-recoil signals from the neutrons are included in the correlation plot of fig. 20. The HERMES scheme was used with an event-to-event coupling of the neutrons produced and transported by the HET-KFA code with the analog MORSE-KFA code. A kB-parameter of 0.85×10^{-2} g cm^{-2} MeV^{-1} was used.

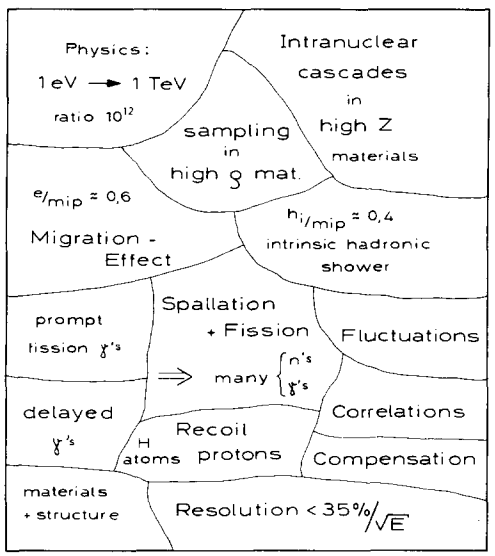

Fig. 22. The "puzzle" of physics between TeV and eV summarizes the phenomena in the hadron sampling calorimetry.

Acknowledgements

We are very much indebted to P. Cloth, D. Filges, Ch. Reul and G. Sterzenbach (IRE, Kernforschungsanlage Jülich, FRG) for the very profitable collaboration which developed in the course of this work. Their former experiences with the HET and MORSE code allowed them to implement many improvements with the aim to adapt a whole code system to future questions of calorimetry.

The big efforts of R. Beckmann and U. Brandenburg in programming and testing the DYMO code are very gratefully acknowledged.

Finally we are very much indebted to Mrs. M. Berghaus for carefully preparing all the drawings and typing of the manuscript.

References

[1] W. Lohmann, R. Kopp and R. Voss, Energy Loss of Muons in the Energy Range 1-10000 GeV, CERN 85-03, Geneva (1985).
[2] C.W. Fabjan, Calorimetry in High-Energy Physics, CERN-EP/85-54, Geneva (1985) fig. 11.
[3] A.J. Lankford, Thesis Geneva (1978) CERN Internal Report EP78-3.
[4] T. Kondo, H. Iwasaki, Y. Watanabe and T. Yamanaka, 1984 Summer Study on the Design and Utilization of the Super Conducting Super Collider, Snowmass, Colorado (June 1984).
[5] J. Brau, Proc. Workshop on Compensated Calorimetry, Pasadena (Sept. 1985) CALT-68-1305.
[6] W. Flauger, Nucl. Instr. and Meth. A241 (1985) 72.
[7] C.W. Fabjan, Proc. of the Wire Chamber Conf. Vienna 1986, Nucl. Instr. and Meth. A252 (1986) 145.
[8] H. Brückmann, Proc. Workshop on Compensated Calorimetry, Pasadena (Sept. 1985) CALT-68-1305.
[9] K. Pinkau, Phys. Rev. B139 (1965) 1548; C.J. Crannell, H. Crannell, C.R. Gillespie, K. Pinkau and R.R. Whitney, Phys. Rev. 182 (1969) 1435 and 1441; H.L. Beck, Nucl. Instr. and Meth. 91 (1971) 525.
[10] D.W.O. Rogers, Nucl. Instr. and Meth. 199 (1982) 531; D.W.O. Rogers, Nucl. Instr. and Meth. A227 (1984) 535.
[11] A.F. Bielajew, D.W.O. Rogers and A.E. Nahum, Phys. Med Biol. 30 (1985) 419 and 429.
[12] W.R. Nelson, H. Hirayama and D.W.O. Rogers, The EGS4 Code System, SLAC-Report-265 (Dec. 1985).
[13] J.B. Birks, Scintillation Counters (McGraw Hill, New York, 1953).
[14] B. Anders, H. Brückmann, γ-Efficiencies in Calorimeter Stacks, ZEUS-Note, to be published, and Jahresbericht, I. Institut für Experimentalphysik 1984/85, Universität Hamburg, FRG.
[15] P. Cloth, D. Filges, G. Sterzenbach, T.W. Armstrong and B.L. Colborn, The KFA-Version of the High-Energy Transport Code HETC and the Generalized Evaluation Code SIMPEL, KFA-Report JUEL-Spez-196, Jülich (March 1983); T.W. Armstrong, P. Cloth, D. Filges and R.D. Neef, Nucl. Instr. and Meth. 222 (1984) 540.
[16] T.W. Armstrong and K.C. Chandler, HETC, Monte Carlo High-Energy Nucleon Meson Transport Code, ORNL-4744 (1972), and Nucl. Sci. Eng. 49 (1972) 110; T.A. Gabriel, The High-Energy Transport Code HETC, ORNL/TM-9727 (Sept. 1985); T.A. Gabriel, Proc. Workshop on Compensated Calorimetry, Pasadena (Sept. 1985) CALT-68-1305.
[17] M.B. Emmett, The MORSE Monte Carlo Radiation Transport Code System, ORNL-4972/R1 (Feb. 1983).
[18] W.W. Engle, Jr., A Users Manual for ANISN, ORNL-CCC254 (June 1973).
[19] U. Brandenburg, Diploma Thesis, Hamburg (1986).
[20] B. Anders, R. Beckmann, U. Brandenburg and H. Brückman, Jahresbericht I. Institut für Experimentalphysik 1984/85, Universität Hamburg, FRG.
[21] R. Kinsey, Data Formates and Procedures for the Evaluated Nuclear Data File ENDF (Oct. 1979).
[22] RSIC Data Library Collection, FEWG1, ORNL-DLC31.
[23] P. Cloth, D. Filges, Ch. Reul and G. Sterzenbach, KFA-Report, in preparation.
[24] R. Beckmann, U. Brandenburg, H. Brückmann, J.M. Hirschberg, M. Obenauf, V. Stieber and K. Wick, Jahresbericht I. Institut für Experimentalphysik 1984/85, Universität Hamburg, FRG.
[25] C. Leroy, Y. Sirois and R. Wigmans, An Experimental Study of the Contribution of Nuclear Fission to the Signal of Uranium Hadron Calorimeters, CERN-EP/86-66 (CERN/EF 86-11) (June 1986).
[26] H. Tiecke, these Proceedings (3rd Pisa Meeting of Advanced Detectors, Castiglione, 1986) Nucl. Instr. and Meth. A263 (1988) 94.
[27] R. Wigmans, Proc. Workshop on Compensated Calorimetry, Pasadena (Sept. 1985) CALT-68-1305.
[28] B. Anders et al., ZEUS Collab., DESY-Report 86-105.
[29] A. Nigro, these Proceedings (3rd Pisa Meeting on Advanced Detectors, Castiglione, 1986) Nucl. Instr. and Meth. A263 (1988) 102.
[30] J. Engler, Calorimetry with Room Temperature Liquids, DESY-HERA 85/01, Geneva (Oct. 1984).